Supplementary Information for

Lifetime Leveraging of Semiconductor Heterostructured and Doped ZnCdS Nanoparticles for Photochemical H_2 Production

Mathew T. Fortunato[a], Joseph M. O'Shea[b], Jie Huang[a], Hashini Chandrasiri[b], Eun Byoel Kim[b], Abdelqader M. Jamhawi[b], A. Jean-Luc Ayitou[b], Preston T. Snee*[b], and Clauria Turro*[a]*

[a] Department of Chemistry, The Ohio State University, 4109 Newman & Wolfrom Laboratory 100 W 18th Ave, Columbus, OH 43210, United States

[b] Department of Chemistry, University of Illinois Chicago, 845 W. Taylor Street, Chicago, Illinois 60607-7061, United States

*E-mail: sneep@uic.edu, turro@ohsu.edu

Chemicals

Cadmium acetate (purum, >98%), (1,5-cyclooctadiene)dimethylplatinum(II) (97%), diphenylphosphine (98%), dodecylamine (98%), diethyl zinc (Et_2Zn, 95%), hexamethyldisilathiane ($(TMS)_2S$, 95%), 11-mercaptoundecanoic acid (95%), 1-octadecene (ODE, 90%), oleic acid (90%), oleylamine (90%), palladium acetate (99.9+%), trioctylamine (98%), sulfur (99.98%), and zinc oxide (ZnO, nanopowder) were purchased from Sigma-Aldrich. Solvents n-hexane (>98.5%), isopropanol (>99.5%), methanol (99.9%), and toluene were from Fisher Scientific. Cadmium oxide brown (CdO, ≥99.0%) was purchased from Fluka, and zinc acetate (99%) was from Acros. Trioctylphosphine (TOP, 97%) was obtained from Strem, and hexadecylamine (>95%) was purchased from TCI. Et_2Zn and $(TMS)_2S$ were stored at -10 ºC in an inert N_2 atmosphere glove box. Oleic acid was recrystallized prior to use.[1] Hexyl phosphonic acid and octadecyl phosphonic acid were prepared according to ref. 2. Oleylamine was purified by vacuum distillation over KOH and was stored under an inert atmosphere. All other reagents were used without further purification. Spectra/Por Float-A-Lyzer G2 300KDa MWCO dialysis tubes were from Spectrum Laboratories, Inc.

Instrumentation

Morphological investigations of the different QD samples were carried out on a JEOL JEM-3010 transmission electron microscope operating at 300 kV. Diluted samples were drop cast and dried on carbon coated gold grids from Ted Pella.

Fluorescence spectra were recorded using a HORIBA FluoroMax-4 spectrofluorimeter. UV/Vis spectroscopy measurements were performed with a Varian Cary 300.

XPS data (survey spectra and elemental composition) were obtained with a Kratos Axis-165. The instrument uses a monochromatic Al Kα (1486.6 eV) X-ray source with an 80 eV pass energy to produce 3 mA emission at a 400 µm spot size. The spectra were obtained at a 0.1 step size with 0.45 eV energy resolution. A 180°, 165 mm hemispherical analyzer was utilized at a take-off angle of 90°.

Time resolved photoluminescence measurements were performed using an Edinburgh Instruments FLS1000 spectrometer equipped with an EPL-450 picosecond pulsed laser diode for excitation. Time resolved absorption measurements were performed on an integrated Helios and EOS system from Ultrafast Systems. The apparatus utilizes a ytterbium femtosecond laser (Hyperion, Ultrafast Systems) with a fundamental at 1030 nm, a pulse duration ~290 fs, and repetition rates of 2.14 kHz for the femtosecond experiments and 1.0 kHz for the nanosecond experiments. The pump beam was generated using a three-stage optical parametric amplifier (Apollo-Y, Ultrafast Systems) with pulse duration ranging from 100–400 fs. The femtosecond broadband probe extending between 360 and 500 nm was generated by focusing the second harmonic of the Hyperion at 515 nm into a thin sapphire plate. A second broadband probe extending between 500 and 910 nm was generated by focusing the 1030 nm laser fundamental into a 1 cm sapphire plate. Probe beams were steered through a Smart Delay Line^{TM} (Ultrafast Systems) to scan the time domain with a delay window of ~7.5 ns and a minimum step size of ~3 fs. The nanosecond probe was generated using a separate supercontinuum laser (MOPA-based, Ultrafast Systems) with a pulse duration of ~0.75 ns. The pump-probe delay was generated electronically in the nanosecond transient absorption experiments. All probes were split into two separate beams, one of which was steered directly onto the reference detector and the other was steered through the sample compartment onto the signal detector.

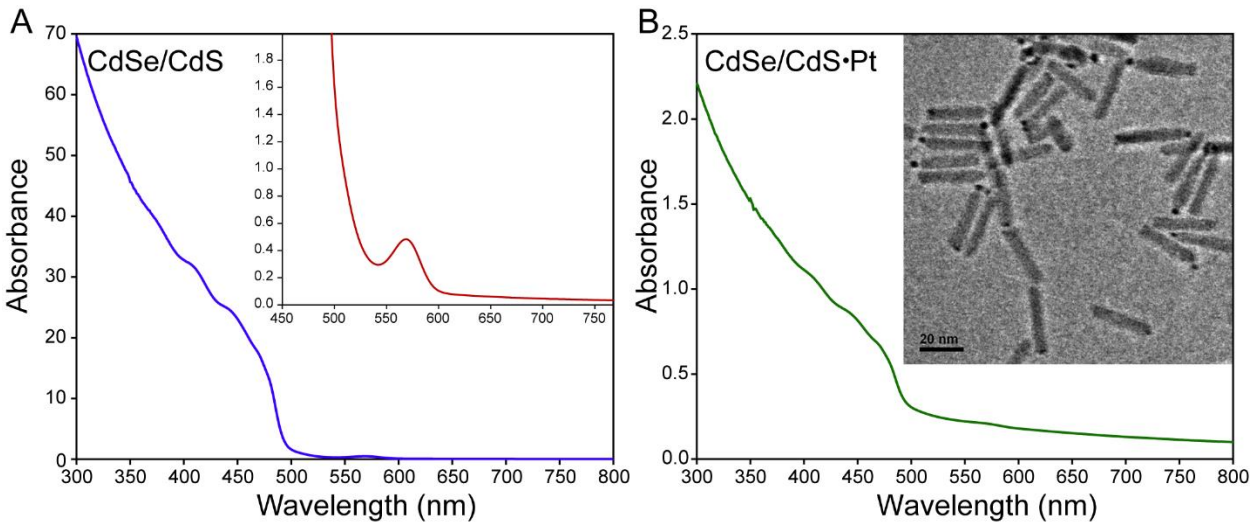

Figure S1. A. Absorption of CdSe/CdS dot-in-rod nanoparticles. Inset: absorption in the bandgap region of the core. **B.** Absorption of the same after thermochemical tipping with platinum nanoparticles. Inset: TEM micrograph of the CdSe/CdS·Pt photocatalysts.

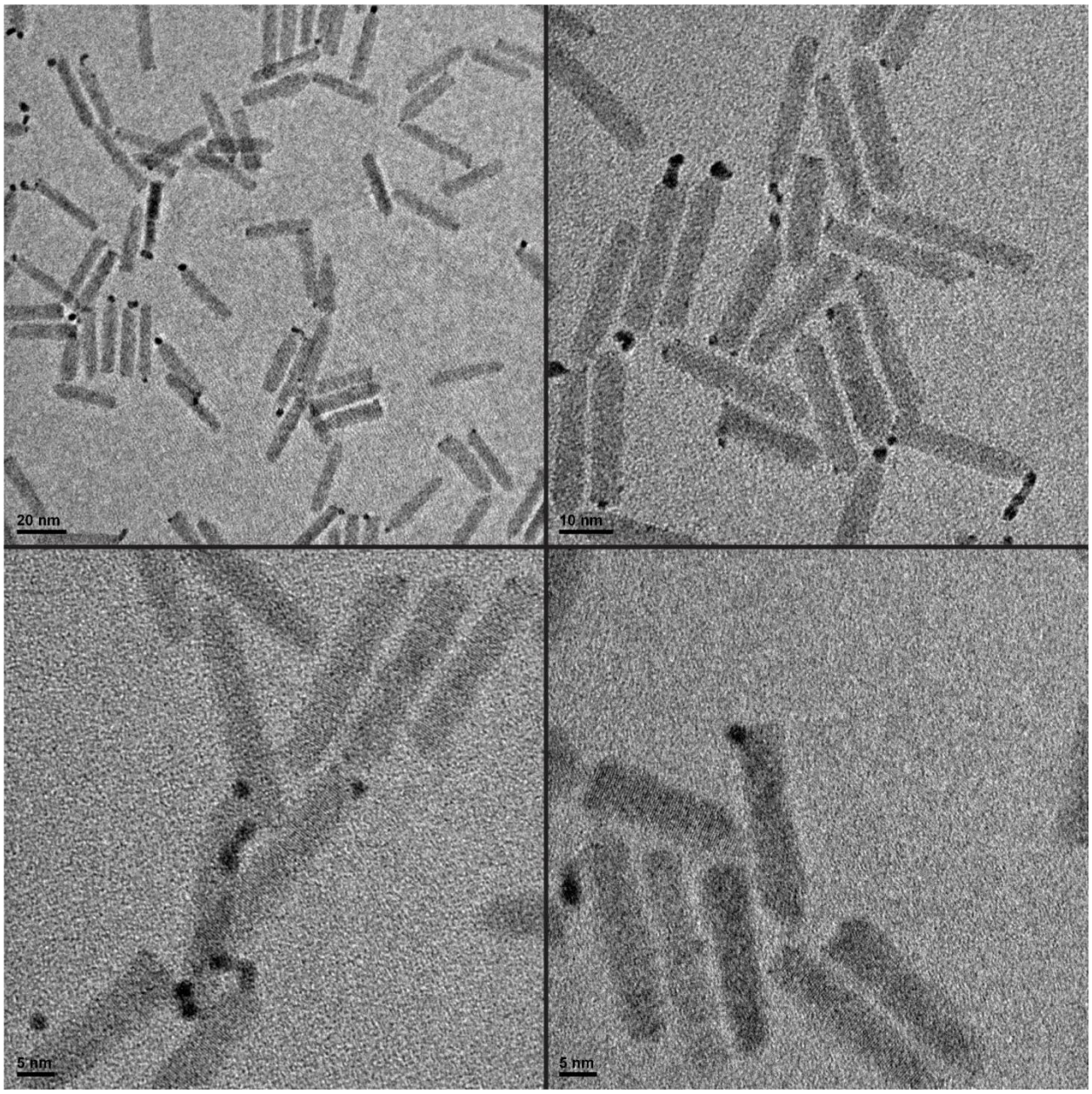

Figure S2. TEM micrographs of CdSe/CdS·Pt photocatalysts.

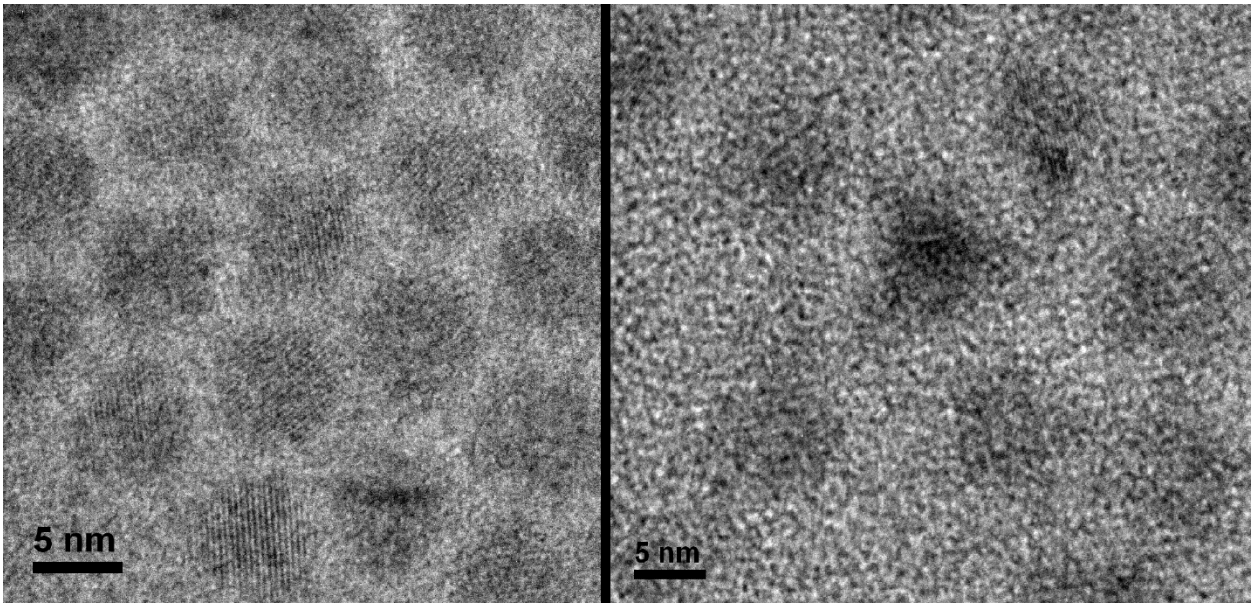

Figure S3. TEM micrographs of **A.** small bandgap ZnCdS and **B.** ZnCdS/ZnS NPs. The larger size of the core/shell is difficult to discern. Coupled with the loss of resolution of the XRD diffractograms shown in Figure S8, the addition of a shell reduces the crystallinity of the nanoparticles.

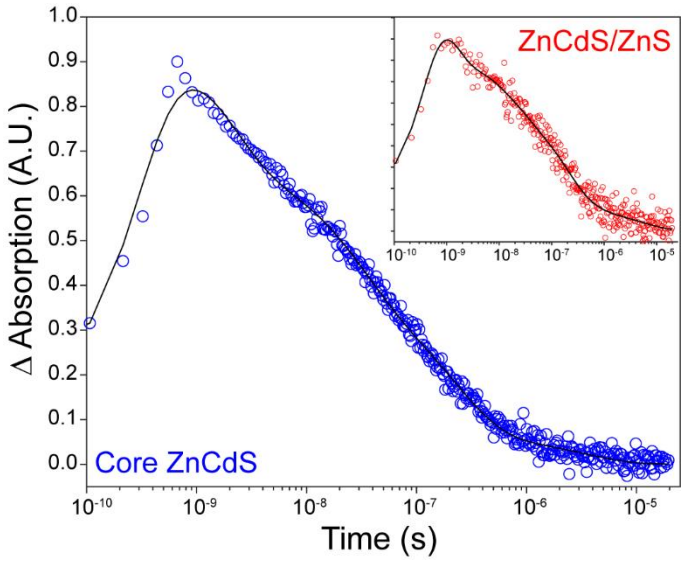

Figure S4. Time resolved absorption kinetics in the low energy region (>500 nm) of large bandgap ZnCdS and (inset) ZnCdS/ZnS NPs reveal the dynamics of trapped electrons. Kinetic parameters are provided in Table S1.

Table S1. Multiexponential fitted parameters for time resolved absorbance data of large bandgap (450 nm) ZnCdS and ZnCdS/ZnS nanoparticles in water shown in Figure 3 of the main text, as well as the transient absorption data of trapped state electrons shown in Figure S3.

	ZnCdS parent	ZnCdS trap e⁻ [a]	ZnCdS/ZnS parent	ZnCdS/ZnS trap e⁻ [a]
A_1	0.1436 ± 0.0009	-	0.0952	-
T_1	16.3 ± 0.3 ps	-	0.199 ps	-
A_2	0.2026 ± 0.0005	0.35 ± 0.05	0.2357 ± 0.0008	0.5 ± 0.7
T_2	0.567 ± 0.007 ns	1.56 ± 0.16 ns	0.256 ± 0.003 ns	0.6 ± 0.3 ns
A_3	0.2477 ± 0.0004	0.273 ± 0.012	0.1860 ± 0.0005	0.3 ± 0.1
T_3	12.91 ± 0.15 ns	25 ± 2 ns	8.68 ± 0.15 ns	5 ± 3 ns
A_4	0.3524 ± 0.0004	0.317 ± 0.012	0.3692 ± 0.0005	0.190 ± 0.008
T_4	159.3 ± 1.1 ns	207 ± 15 ns	131.3 ± 0.9 ns	160 ± 20 ns
A_5	0.0537 ± 0.0005	0.061 ± 0.006	0.1139 ± 0.0004	0.037 ± 0.006
T_5	1.87 ± 0.14 µs	3.1 ± 0.5 µs	1.56 ± 0.03 µs	4.6 ± 1.9 µs
<t>	160 ± 6 ns	260 ± 40 ns	228 ± 4 ns	204 ± 150 ns

a. Net absorption > 500 nm. These features could not be observed at early times using our time resolved laser system.

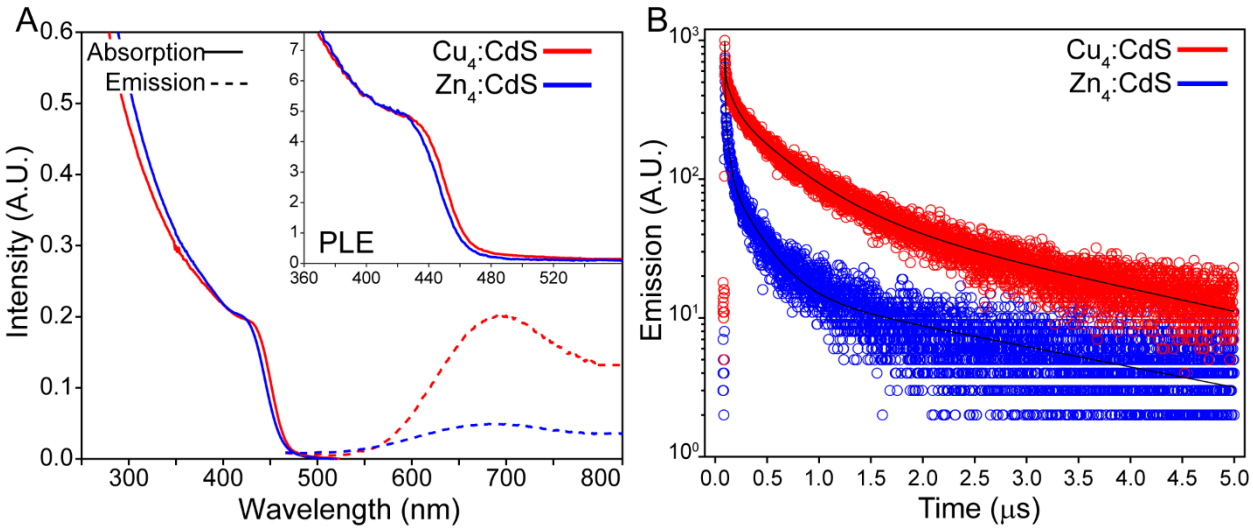

Figure S5. A. Absorption of exactly doped Cu_4:CdS and Zn_4:CdS NPs. Inset: photoluminescence excitation (PLE) of the same samples. **B.** Time resolved 730 nm emission (450 nm excitation) of Cu_4:CdS and control Zn_4:CdS NPs. The data were fit with convolution of the instrument response function; results are provided in Table S2. The data reveal a ~4.5 fold longer lifetime of the copper doped samples relative to the control.

Table S2. Multiexponential fitted parameters for time resolved emission parameters of deep trap emission from Zn_4:CdS and phosphorescence of doped Cu_4:CdS nanoparticles.

Sample	A_1	τ_1 (ns)	A_2	τ_2 (ns)	A_3	τ_3 (ns)	A4	τ 4 (ns)	τ_{avg} (ns)
Zn_4:CdS	0.70 ±0.04	3.0±0.4	0.21 ±0.02	34.1±3	0.081 ±0.004	261±12	0.0146 ±0.0005	2962 ±100	74±4
Cu_4:CdS	0.46 ±0.04	6.0±0.8	0.21± 0.01	81±7	0.258± 0.005	512±17	0.068± 0.003	2690 ±90	335±15

Size selective precipitation. Small and large bandgap ZnCdS/ZnS·Pd nanoparticles (NPs) were precipitated by addition of small portions of isopropanol and/or methanol while stirring, which was halted after precipitation was observed. The samples were centrifuged, and the supernatant was characterized by absorption. The precipitate was resuspended in hexane and was also interrogated by UV/Vis absorption spectroscopy.

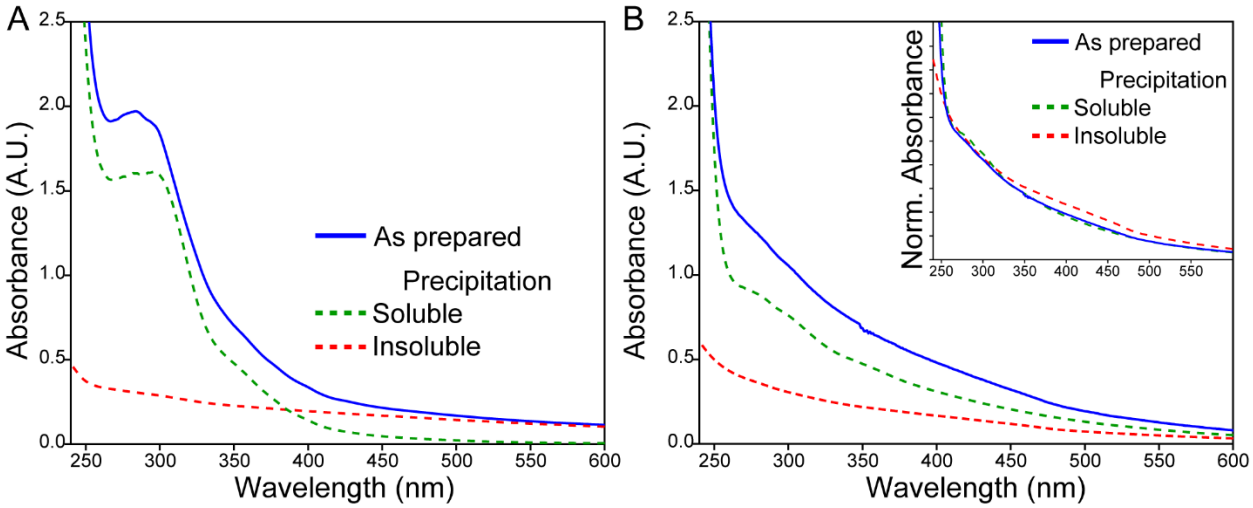

Figure S6. A. Spectrum of large bandgap (450 nm) ZnCdS/ZnS·Pd NPs (blue line) prepared by high temperature thermolysis using an overabundance of Pd salt precursors. Size selective precipitation yields a soluble portion (green dash) that has semiconductor features. The resuspended precipitate has a flat spectrum (red dash) and is most likely due to free Pd nanoparticles. **B.** Spectrum of large bandgap (450 nm) ZnCdS/ZnS·Pd NPs after optimization of the precursor to ZnCdS/ZnS NP ratio. Inset: the normalized spectra of the sample, supernatant, and the resuspended precipitate are all qualitatively similar, indicating greater homogeneity on a per-particle basis.

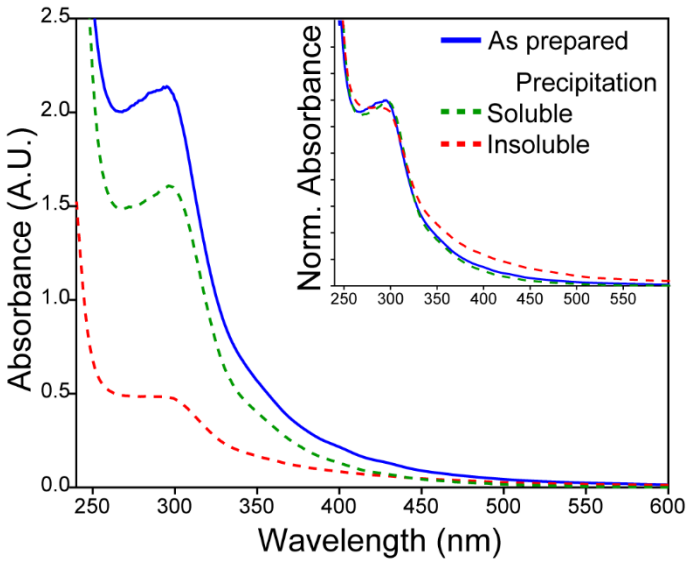

Figure S7. Spectrum of small bandgap (485 nm) ZnCdS/ZnS·Pd NPs after optimization of the precursor to ZnCdS/ZnS NP ratio and temperature. Inset: the normalized spectra of the sample, supernatant, and the resuspended precipitate are all qualitatively similar, indicating greater homogeneity on a per-particle basis.

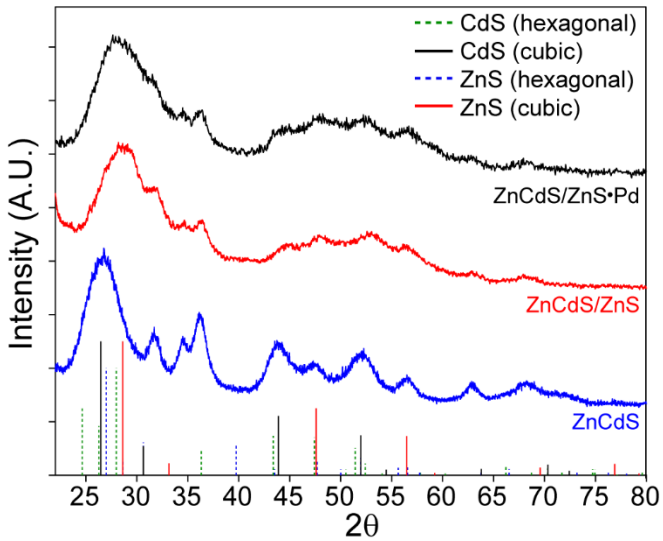

Figure S8. XRD of small bandgap (485 nm) ZnCdS, ZnCdS/ZnS, and ZnCdS/ZnS·Pd, with references for cubic and hexagonal CdS and ZnS shown. The spectra appear to be composed of a dominant ZnS component with CdS, with most features appearing consistent with the cubic form. The addition of a ZnS shell onto the ZnCdS core broadens the resonances, which is due to a loss of crystallinity.

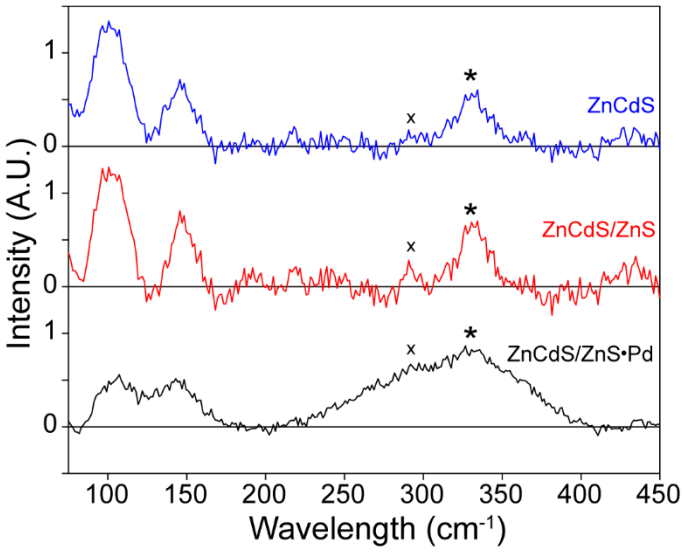

Figure S9. Raman spectra of low bandgap core ZnCdS, core/shell ZnCdS/ZnS, and ZnCdS/ZnS·Pd adducts reveals a consistent 331 cm^{-1} peak (*) that can be attributed to a $Zn_{0.7}Cd_{0.3}S$ according to a calibration to the data of ref. 3. This composition is nearly identical to that found in an earlier study (ref. 4) of the same materials. The 291 cm^{-1} feature (×) is attributable to CdS, while the lower energy 100 cm^{-1} and 147 cm^{-1} peaks are most likely due to ligands. The increase in the relative intensity of the ~290 cm^{-1} feature is attributed to etching of the nanomaterial due to the photochemical process of palladium adduct formation.

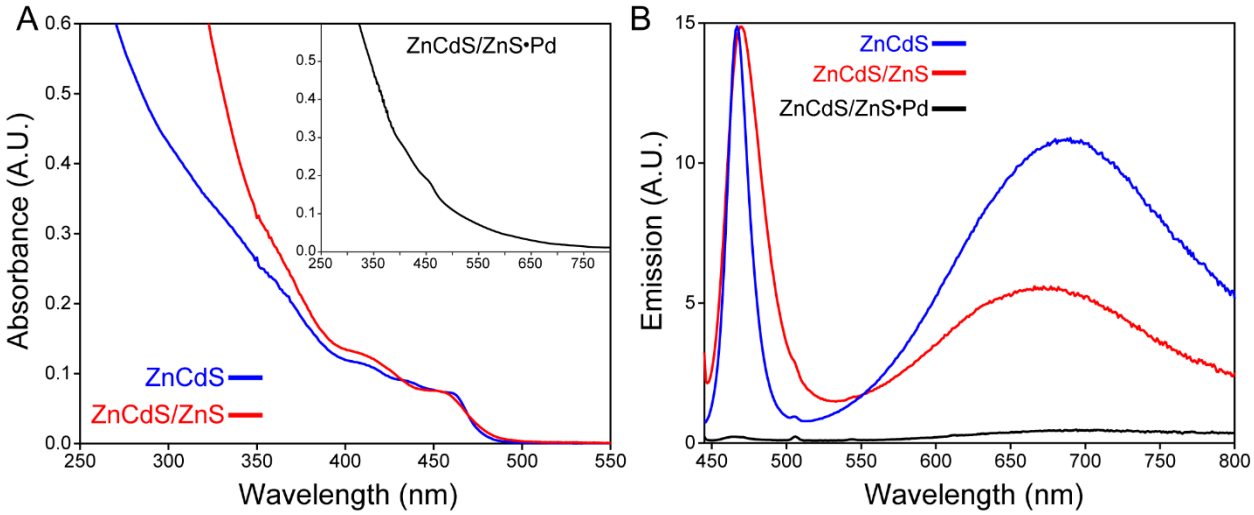

Figure S10. A. Absorption spectra of low bandgap (485 nm) ZnCdS, ZnCdS/ZnS, and ZnCdS/ZnS·Pd NPs. **B.** Emission of core and core/shell nanoparticles reveals suppression of trap state emission in the NIR, while the conjugation of a Pd adduct results in substantial quenching due to charge carrier separation.

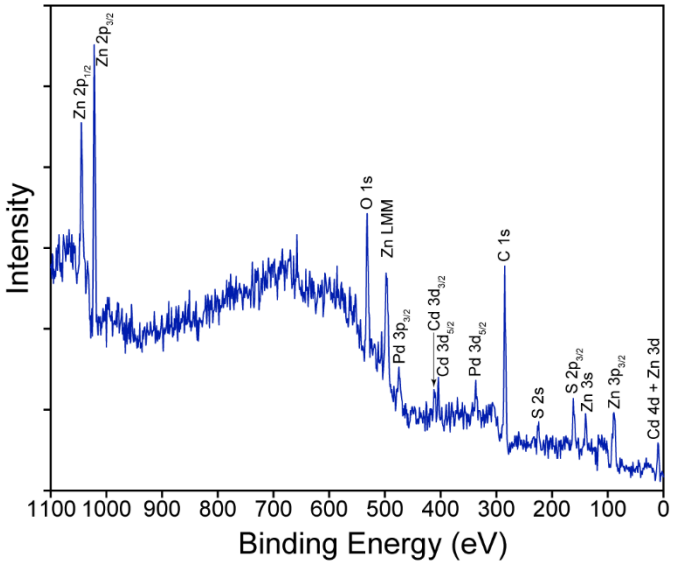

Figure S11. XPS survey spectrum of low bandgap (485 nm) ZnCdS/ZnS·Pd NPs reveals the presence of Zn, Cd, S, and Pd.

Table S3. Elemental composition of low bandgap (485 nm) ZnCdS/ZnS·Pd NPs from XPS measurements.

Peak	Position BE (eV)	FWHM (eV)	Raw Area (CPS)	RSF	Atomic Mass	Atomic Conc %	Mass Conc %
O 1s	532	3.951	1339.9	0.780	15.999	45.50	21.42
Zn 2p	1022	3.413	4576.2	5.589	65.387	17.54	33.74
S 2p	162	4.692	814.0	0.668	32.065	32.57	30.73
Cd 3d	404	2.440	518.6	6.623	112.422	2.13	7.05
Pd 3d	337	4.307	442.1	5.356	106.534	2.25	7.06

Parameter set for Tight Binding calculations.

The tight binding method was employed to simulate large semiconductor heterostructures. This theory creates a single Hamiltonian matrix that describes the energetics of electrons hopping from an atomic site to the four nearest neighbors. Surface states created by atoms missing a full set of bonding partners were suppressed by raising those sites' energies as per ref. 5. One issue to address is that the bands derived from published parameter sets have E=0 eV defined at the Γ point valence band maxima. Thus, their use unmodified would not capture the intrinsic preference for a charge carrier to sequester within one bulk material or the other. As a result, the parameters were modified to impart a relative alignment with the proper bandgaps while minimizing the overall perturbation to the entire solid state band structure.

CdSe: The parameter set by ref. 6 was allowed to retain a valence band maximum at 0 eV while setting the direct bandgap conduction minimum to 1.764 eV.

CdS: The parameter set of ref. 7 was modified to set the valence band maximum to -0.4065 eV and the conduction band maximum to 1.99 eV (2.396 eV bandgap).

Table S4. Tight binding parameter sets for CdSe and CdS adjusted to conform to the relative band alignments of the bulk. All energies in eV.

	CdSe (eV)	CdS (eV)
E(s,a)	-9.656	-11.9927
E(p,a)	1.3000	0.0673
E(s,c)	-0.0372	1.3459
E(p,c)	4.6628	5.3859
E(s*,a)	7.5040	6.6673
E(s*,c)	5.6528	6.3859
V(s,s)	-1.1248	-0.7500
V(x,x)	0.6267	0.4255
V(x,y)	1.3113	1.0473
V(sa,pc)	1.0769	0.4949
V(sc,pa)	1.3456	1.3573
V(s*a,pc)	0.7537	0.4955
V(s*c,pa)	0.6195	0.7602

WKB Approximation on tunneling probability.

Wentzel–Kramers–Brillouin theory[8] determines a transmission coefficient using the formula:

$$T = e^{-2\cdot\sqrt{\frac{2m\cdot U}{\hbar^2}}\cdot L}$$

Inserting $L = 10 \times 10^{-9}$m, $\hbar = 1.0546 \times 10^{-34}$ J · s, $m = m_0 \cdot m_{e/h}$, where $m_0 = 9.109 \times 10^{-34}$kg, $m_e = 0.13$, $m_h = 0.5$, $U_e = 0.2973$ eV $= 4.763 \times 10^{-20}$ J, and $U_h = 0.3189$ eV $= 5.109 \times 10^{-20}$ J yields a tunneling probability of T_e=0.5289 for the electron and and T_h= 0.2742 for the hole. Increasing the length widens the ratio of the transmission probability further, reaching ~700× for L=100 nm.

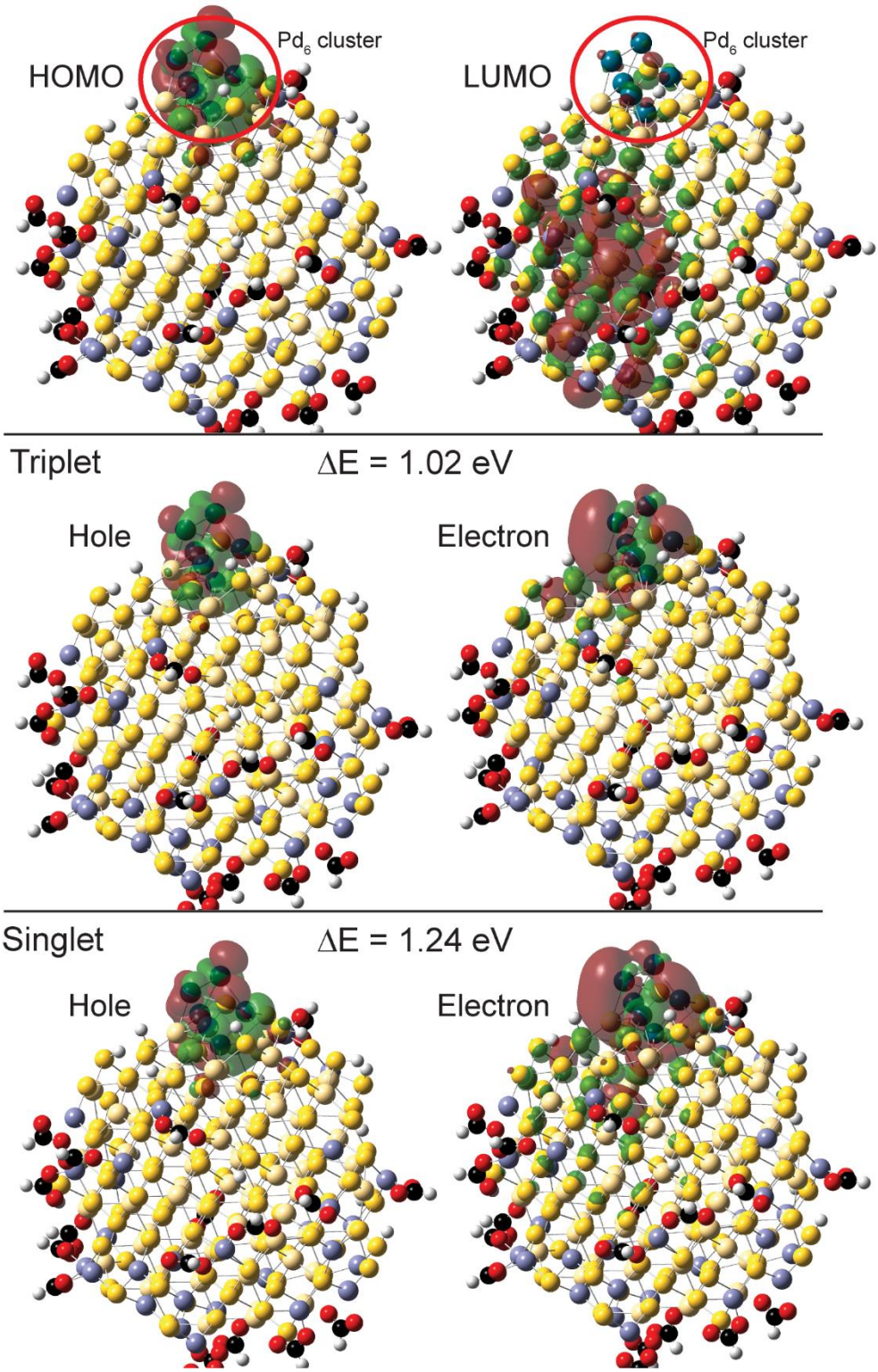

Figure S12. DFT (PBE1PBE/LANL2DZ) HOMO – LUMO orbitals of $(HCO_2H)_{18}Zn_{30}Cd_{84}S_{114}{\cdot}Pd_6$, as well as the lowest excited state (triplet) and the first optically allowed singlet states from TDDFT/NTO analysis. The NTO orbitals have greater overlap with the host semiconductor compared to the platinum states shown in Figure S13.

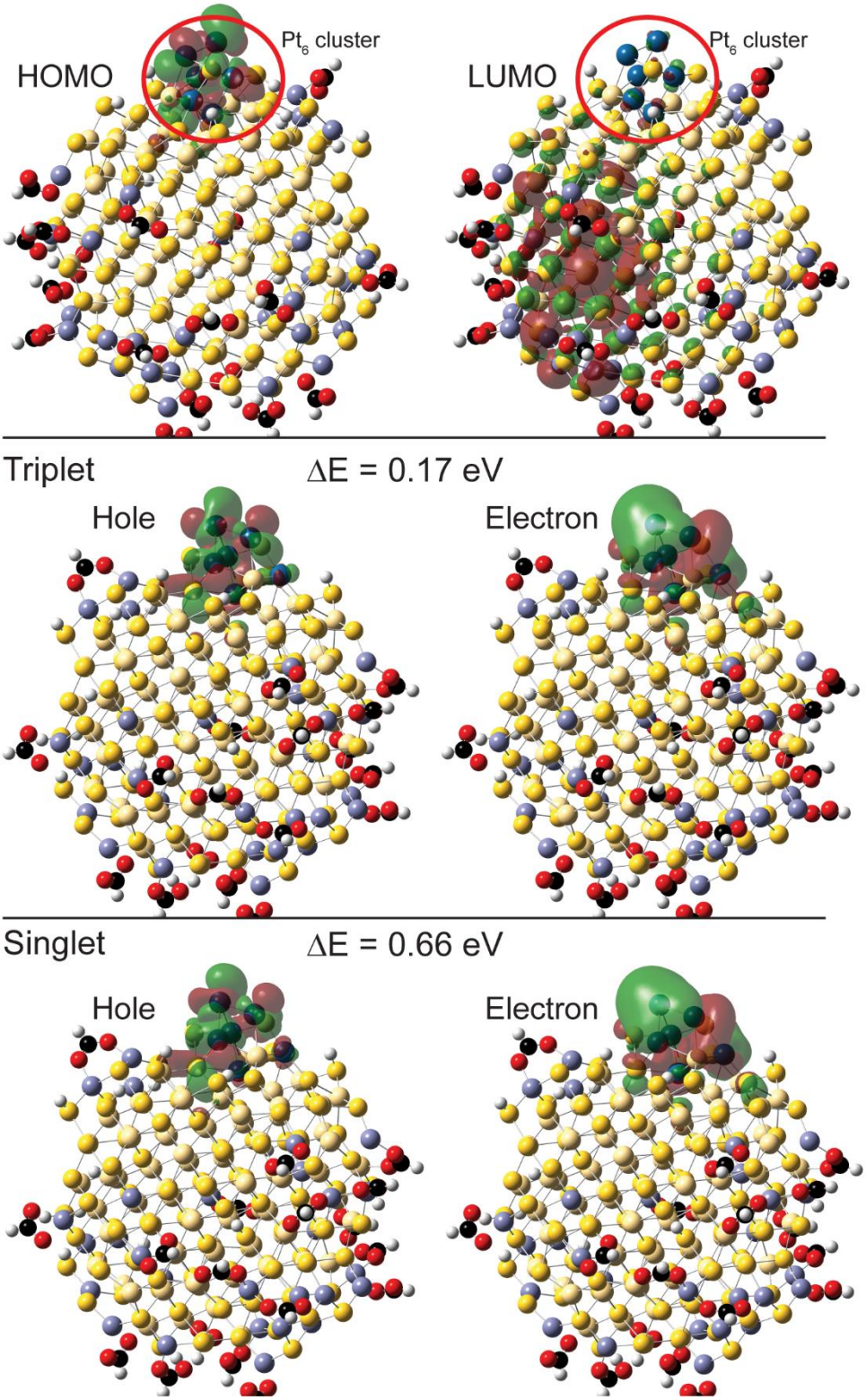

Figure S13. DFT (PBE1PBE/LANL2DZ) HOMO – LUMO orbitals of $(HCO_2H)_{18}Zn_{30}Cd_{84}S_{114}{\cdot}Pt_6$, as well as the lowest excited state (triplet) and the first optically allowed singlet states from TDDFT/NTO analysis.

References

1 R. L. Arudi, M. W. Sutherland and B. H. Bielski, *J. Lipid. Res.*, 1983, **24**, 485–488.

2 G. M. Kosolapoff, *J. Am. Chem. Soc.*, 1945, **67**, 1180–1182.

3 R. Sethi, P. K. Sharma, A. C. Pandey and L. Kumar, *Chemical Physics Letters*, 2010, **495**, 63–68.

4 L. E. Page, X. Zhang, C. M. Tyrakowski, C.-T. Ho and P. T. Snee, *Analyst*, 2016, **141**, 6251–6258.

5 S. Lee, F. Oyafuso, P. von Allmen and G. Klimeck, *Phys. Rev. B*, 2004, **69**, 045316.

6 P. E. Lippens and M. Lannoo, *Phys. Rev. B*, 1990, **41**, 6079–6081.

7 P. E. Lippens and M. Lannoo, *Phys. Rev. B*, 1989, **39**, 10935–10942.

8 J. J. Sakurai, *Modern Quantum Mechanics, Revised Edition*, Pearson.